LETTER

doi:10.1038/nature10975

# Exploiting a natural conformational switch to engineer an interleukin–2 'superkine'

Aron M. Levin[1]*, Darren L. Bates[2]*, Aaron M. Ring[2]*, Carsten Krieg[3,4]*, Jack T. Lin[5], Leon Su[5], Ignacio Moraga[2], Miro E. Raeber[3,4], Gregory R. Bowman[6], Paul Novick[6], Vijay S. Pande[6], C. Garrison Fathman[5], Onur Boyman[3,4] & K. Christopher Garcia[1,2]

**The immunostimulatory cytokine interleukin-2 (IL-2) is a growth factor for a wide range of leukocytes, including T cells and natural killer (NK) cells[1–3]. Considerable effort has been invested in using IL-2 as a therapeutic agent for a variety of immune disorders ranging from AIDS to cancer. However, adverse effects have limited its use in the clinic. On activated T cells, IL-2 signals through a quaternary 'high affinity' receptor complex consisting of IL-2, IL-2Rα (termed CD25), IL-2Rβ and IL-2Rγ[4–8]. Naive T cells express only a low density of IL-2Rβ and IL-2Rγ, and are therefore relatively insensitive to IL-2, but acquire sensitivity after CD25 expression, which captures the cytokine and presents it to IL-2Rβ and IL-2Rγ. Here, using *in vitro* evolution, we eliminated the functional requirement of IL-2 for CD25 expression by engineering an IL-2 'superkine' (also called super-2) with increased binding affinity for IL-2Rβ. Crystal structures of the IL-2 superkine in free and receptor-bound forms showed that the evolved mutations are principally in the core of the cytokine, and molecular dynamics simulations indicated that the evolved mutations stabilized IL-2, reducing the flexibility of a helix in the IL-2Rβ binding site, into an optimized receptor-binding conformation resembling that when bound to CD25. The evolved mutations in the IL-2 superkine recapitulated the functional role of CD25 by eliciting potent phosphorylation of STAT5 and vigorous proliferation of T cells irrespective of CD25 expression. Compared to IL-2, the IL-2 superkine induced superior expansion of cytotoxic T cells, leading to improved antitumour responses *in vivo*, and elicited proportionally less expansion of T regulatory cells and reduced pulmonary oedema. Collectively, we show that *in vitro* evolution has mimicked the functional role of CD25 in enhancing IL-2 potency and regulating target cell specificity, which has implications for immunotherapy.**

To engineer a CD25-independent version of IL-2, we displayed human IL-2 on the surface of yeast as a conjugate to Aga2p, and verified proper receptor-binding properties with IL-2Rβ and IL-2Rγ ectodomain tetramers that were carboxy-terminally biotinylated and coupled to phycoerythrin-conjugated streptavidin for use as a staining and sorting reagent[9,10]. Yeast-displayed IL-2 bound to IL-2Rγ in the presence of IL-2Rβ, recapitulating the cooperative assembly of the heterodimeric receptor complex as seen with soluble IL-2 (Fig. 1a and Supplementary Fig. 1). We proceeded to carry out two generations of *in vitro* evolution (Fig. 1b and Supplementary Fig. 2). Our first generation *in vitro* evolution strategy was to create an error-prone PCR library of the entire IL-2 coding sequence (Supplementary Fig. 2), which resulted in selection of a predominant IL-2 variant containing an L85V mutation (Fig. 1c and Supplementary Fig. 3).

From inspection of the wild-type (WT) IL-2 structure, we were surprised to find that position 85 was not a direct IL-2Rβ contact residue, but rather resided on the internal face of the IL-2 C-helix, within the hydrophobic core of the cytokine (Fig. 2a). Thus, we surmised

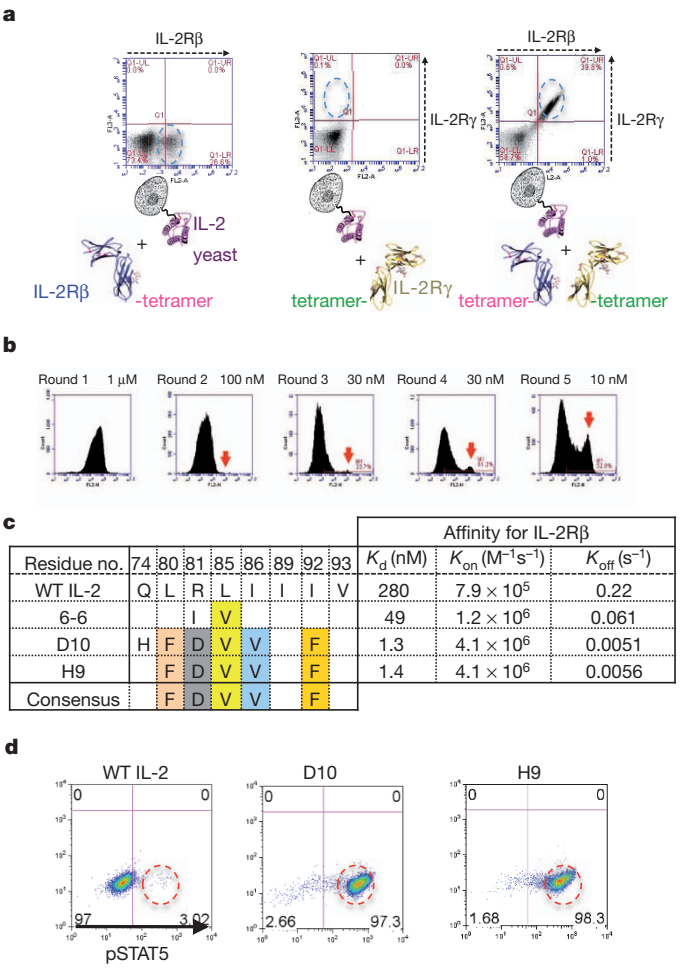


**Figure 1 | *In vitro* evolution of human IL-2 variants with high affinity for IL-2Rβ.** **a**, IL-2 displayed on yeast recapitulates cooperative receptor-binding activity. As measured by flow cytometry, IL-2 binds weakly to IL-2Rβ (left panel), undetectably to IL-2Rγ (middle panel), and cooperatively forms the IL-2Rβ–IL-2Rγ heterodimer (right panel). **b**, Enrichment of IL-2 variants on yeast by selection with progressively lower concentrations of IL-2Rβ. Red arrows indicate an emerging population of high-affinity IL-2Rβ binders (see also Supplementary Fig. 2). **c**, Sequences and affinities for IL-2Rβ of selected mutants from the first (mutant 6-6) and second (mutants D10 and H9) generation libraries (see Supplementary Fig. 3 for an extended table). **d**, On-yeast stimulation of YT-1 cells (human NK cell line) by wild-type (WT) IL-2-yeast and high-affinity variants (IL-2 superkines) (see also Supplementary Fig. 4).

[1]Howard Hughes Medical Institute, Stanford University School of Medicine, Stanford, California 94305, USA. [2]Department of Molecular and Cellular Physiology, and Department of Structural Biology, Stanford University School of Medicine, Stanford, California 94305, USA. [3]Laboratory of Applied Immunobiology, University of Zurich, Zurich CH-8006, Switzerland. [4]Allergy Unit, Department of Dermatology, University Hospital Zurich, Zurich CH-8091, Switzerland. [5]Stanford University School of Medicine, Department of Medicine, Division of Immunology and Rheumatology, Stanford, California 94305, USA. [6]Department of Chemistry, Stanford University, Stanford, California 94305, USA.
*These authors contributed equally to this work.

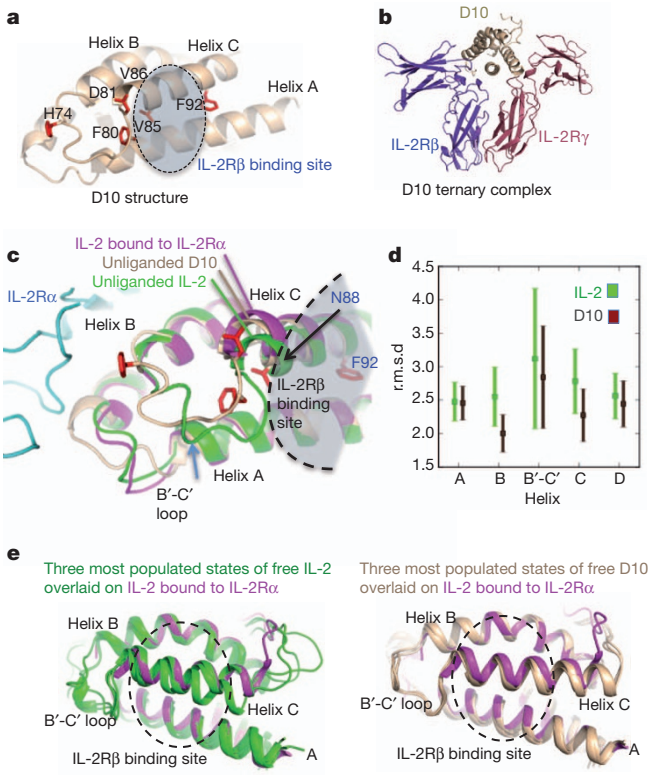


**Figure 2 | Basis of affinity enhancement for IL-2Rβ from structural and molecular dynamics characterization of the D10 IL-2 superkine.** **a**, Crystal structure of the D10 IL-2 superkine at 3.1 Å with mutated residues in red (see also Supplementary Table 1 and Supplementary Fig. 7a). **b**, D10 in complex with human IL-2Rβ and IL-2Rγ preserves the wild-type receptor dimer geometry (see also Supplementary Fig. 7b). **c**, The unliganded D10 IL-2 superkine helix C (brown), moves towards its hydrophobic core compared to unliganded wild-type IL-2 (green, PDB ID 3INK). This helix C position is more similar to that of helix C in IL-2 bound to IL-2Rα (purple, PDB ID 1Z92) (see also Supplementary Fig. 8). **d**, A 40-ns molecular dynamics simulation shows a reduction of the average r.m.s.d. for the B and C helices, and the B-C loop in D10 versus IL-2 (see also Supplementary Fig. 8c). Error bars represent the standard error of the r.m.s.d. **e**, Helix C in IL-2 (green, left panel) drifts during the molecular dynamics simulation more than the IL-2 superkine D10 (brown, right panel) when compared to IL-2 bound to IL-2Rα (purple).

that L85V may affect the structure of helix C in a way that enhances binding to IL-2Rβ. Therefore, we carried out a second generation selection where we made a biased library that contained F/I/L/V at amino acids L80, L85, I86, I89, I92 and V93, which are contained within the hydrophobic core and linker region on helix C (Fig. 1b, c). To rapidly select the most active variants, we used the yeast-displayed cytokines themselves to stimulate STAT5 phosphorylation in the human NK cell line YT-1 by co-incubation at varying yeast:YT-1 cell ratios (Fig. 1d and Supplementary Fig. 4). Several clones stimulated substantially more STAT5 phosphorylation at lower yeast:cell ratios than yeast-displayed wild-type IL-2 (Fig. 1d and Supplementary Fig. 4). Sequencing of a selected panel of high-affinity IL-2 clones revealed a consensus set of mutations L80F/R81D/L85V/I86V/I92F (Fig. 1c and Supplementary Fig. 3).

We expressed recombinant forms of several first- and second-generation IL-2 clones to measure their binding affinities and kinetics for IL-2Rβ by surface plasmon resonance (SPR) (Fig. 1c and Supplementary Figs 3 and 5) and isothermal titration calorimetry (ITC) (Supplementary Fig. 6). By SPR, the affinity between IL-2 and IL-2Rβ was $K_d$ = 280 nM. The IL-2 superkines, also called 'super-2s', clustered into low, medium and high affinity classes. The highest affinity mutants had $K_d$s of 1.2–1.7 nM (D10, H9). The affinity increases were uniformly manifested in reductions in off-rates (Fig. 1c and Supplementary Figs 3 and 5).

To understand the structural consequences of the evolved mutations, we crystallized the D10 IL-2 superkine (Fig. 2a, Supplementary Fig. 7a and Supplementary Table 1). In the structure of D10 alone, five of the six mutations clustered on the B-C loop and within the C-helix core, in positions that did not contact IL-2Rβ. Notably, the B-C-helix linker region was ordered in the electron density map (Supplementary Figs 7a and 8a), compared to other IL-2 structures where this region is often disordered (Supplementary Fig. 8a). Collectively, the F80, V85 and V86 substitutions appeared to collapse into a hydrophobic cluster that stabilized the loop by pinning the C-helix into the core of the molecule. Only one of the five consensus mutations, I92F, was at a position that contacted IL-2Rβ in the receptor complex (Fig. 2a), but it was deeply inserted between the C and A helices, contributing only an additional 10 Å$^2$ of molecular surface buried by IL-2Rβ in the complex compared to Ile 92. We also determined a low-resolution (3.8 Å) structure of the D10 ternary receptor complex to assess whether the mutations have perturbed the IL-2Rβ/IL-2Rγ receptor dimer geometry compared to the wild-type IL-2 complex (Fig. 2b and Supplementary Table 1). The overall IL-2Rβ/IL-2Rγ heterodimeric architecture and mode of cytokine/IL-2Rβ contact in the D10 ternary complex were essentially identical to the previously reported IL-2 quaternary assembly (root mean squared deviation (r.m.s.d.) = 0.43 Å) (Supplementary Fig. 7b).

Previously, we found that the C-helix of IL-2 seems to undergo subtle repositioning upon binding to IL-2Rα[11] (Fig. 2c and Supplementary Fig. 8a). Inspection of three wild-type unliganded IL-2 structures revealed conformational variability in the C-helix position, consistent with higher crystallographic B-factors in this helix relative to the rest of the molecule (Supplementary Fig. 8b). We compared the structure of our D10 IL-2 superkine to that of an unliganded structure of IL-2, and IL-2 in the receptor complexes. We found that the C-helix in D10 was more similar to that seen in the two receptor-bound conformations of IL-2 than the free forms, having undergone a relatively small shift towards the helical core as a consequence of the stabilizing mutations (Fig. 2c).

We used molecular dynamics simulations of IL-2 and D10 to further interrogate the mechanism responsible for higher binding affinity to IL-2Rβ by the IL-2 superkine (Fig. 2d, e). We constructed an atomically detailed Markov state model (MSM) to probe the relative conformational flexibility of IL-2 versus D10 directly. Analysis of the MSM clearly demonstrated that D10 was more stable than IL-2, and that IL-2 visited nearly twice as many clusters as D10. For example, the most populated state of D10 had an equilibrium probability of approximately 0.20, compared to approximately 0.05 for IL-2, demonstrating that the equilibrium population of D10 was far more localized than IL-2. Helix B, the B-C loop and helix C appeared rigidified in D10 compared to IL-2 as evidenced by reduced r.m.s.d. from the starting conformations (Fig. 2d and Supplementary Movies 1, 2). F92 seemed to act as a molecular wedge between helix C and helix A, stabilizing the more C-terminal end of the helix (Fig. 2a). We also simulated both D10 and IL-2 starting in a receptor-bound-like structure and monitored the divergence in r.m.s.d. of the B-C loop and helix C from the actual receptor-bound structure. IL-2 (Fig. 2e, left, and Supplementary Fig. 8c) quickly 'wandered' from the receptor conformation and experienced drastic fluctuations compared to D10 (Fig. 2e, right, Supplementary Fig. 8c and Supplementary Movies 1 and 2). Based on these observations, we propose a mechanism whereby the reduced flexibility of helix C in the IL-2 superkine, as a result of its improved core packing with helix B, results in a superior receptor-binding poise that increases its affinity for IL-2Rβ, and consequently mimics a functional role of CD25. The structural and molecular dynamics results indicate that the evolved mutations in the IL-2 superkine cause a conformational stabilization of the cytokine that reduces the energetic penalties for binding to IL-2Rβ.

We asked if the IL-2 superkines demonstrated signalling potencies on cells in accordance with their IL-2Rβ-binding affinities, and whether their activities depended on cell surface expression of CD25. We determined the dose–response relationships of wild-type IL-2 versus the IL-2 superkines 6-6, D10 and H9 on both $CD25^-$ and $CD25^+$ human YT-1 NK cells by assaying STAT5 phosphorylation with flow cytometry (Fig. 3a–d and Supplementary Fig. 9). On $CD25^-$ YT-1 cells, the half-maximum effective concentration ($EC_{50}$) of H9 and D10 were decreased over tenfold ($EC_{50}$ = 2.5 and 1.8 ng ml$^{-1}$, respectively) compared to IL-2 ($EC_{50}$ = 39 ng ml$^{-1}$), with the 6-6 mutein yielding an $EC_{50}$ intermediate between IL-2 and H9/D10 ($EC_{50}$ = 15 ng ml$^{-1}$), consistent with the improved affinity of the IL-2 superkines for IL-2Rβ (Fig. 3a). On $CD25^+$ YT-1 cells, the $EC_{50}$ of IL-2 decreased over 50-fold relative to $CD25^-$ YT-1 cells, from 39 to 0.66 ng ml$^{-1}$ (Fig. 3b). In contrast, the $EC_{50}$ of H9 and D10 improved only modestly in the presence of CD25 ($EC_{50}$ of 0.47 and 0.52 compared to 2.5 and 1.8 ng ml$^{-1}$, respectively) (Fig. 3b).

We sought to further probe the CD25-independence of the IL-2 superkines by taking advantage of a previously characterized mutation in IL-2, Phe 42 to Ala (F42A), which showed reduced binding to CD25 by approximately 220-fold for H9 ($K_d$ 6.6 nM versus 1.4 μM) and approximately 120-fold for IL-2 ($K_d$ 6.6 nM versus 0.8 μM) (Supplementary Fig. 10)[12,13]. The F42A mutation is an alternative diagnostic probe of the relative CD25 dependence of IL-2 and the IL-2 superkine. The F42A mutation right-shifted the dose–response curve of wild-type IL-2 on $CD25^+$ cells by about 1 log, but had no effect on $CD25^-$ cells (Fig. 3c). In contrast, H9 was far less sensitive to the F42A mutation, with the dose–response curves of H9 versus H9 F42A being very similar on both $CD25^+$ and $CD25^-$ cells (Fig. 3d).

We assessed the activity of several IL-2 superkines on T cells that were either deficient in, or expressed CD25. For the former experiment, $CD4^+$ T cells were isolated from CD25-knockout mice, followed by stimulation by either wild-type IL-2 or six IL-2 superkines and assaying for STAT5 phosphorylation at a range of cytokine concentrations (Fig. 3e and Supplementary Fig. 11). $CD25^{-/-}$ $CD4^+$ T cells responded poorly to exogenous wild-type IL-2 stimulation, but the IL-2 superkines induced STAT5 phosphorylation in these cells proportional to their affinity for IL-2Rβ.

The principle functional effect of IL-2 is to promote T cell proliferation, particularly for naive T cells. Human naive $CD4^+$ T cells were isolated and left either unstimulated or stimulated with plate-bound anti-CD3 antibody with or without the different IL-2 variants (Fig. 3f and Supplementary Fig. 12). Increased proliferation effects on naive human T cells correlated with increased affinity for IL-2Rβ and STAT5 phosphorylation shown earlier, as the rank order of potency was D10 = H9 > 6-6> wild-type IL-2 (see Supplementary Fig. 12 for the complete titration).

We next tested the IL-2 variants for their ability to induce STAT5 phosphorylation on experienced human $CD4^+$ T cells (Supplementary Fig. 13), which highly express the trimeric IL-2Rαβγ complex. Human $CD4^+$ T cells were activated *in vitro* by T cell receptor (TCR) stimulation and rested to generate 'experienced' human $CD4^+$ $CD25^+$ T cells. As for the $CD25^+$ YT-1 cells, we observed a much smaller difference between IL-2 and the IL-2 superkines.

We assessed the potency of the IL-2 superkine H9 on expansion of $CD25^{low}$ versus $CD25^{high}$ T cells, in comparison to wild-type IL-2 and IL-2–anti-IL-2 monoclonal antibody (mAb) complexes, which have been shown to exert reduced pulmonary oedema yet very potent antitumour responses *in vivo*[14–16]. On antigen-experienced (memory-phenotype, MP) $CD8^+$ T cells, expressing only low levels of CD25 but high levels of IL-2Rβγ, H9 induced more than three times the rate of proliferation and expansion as wild-type IL-2 (Fig. 4a and Supplementary Fig. 14a). However, on $CD4^+$ $CD25^{high}$ T regulatory ($T_{reg}$) cells, we found that the CD25-competent wild-type IL-2 and H9 achieved comparable maximal expansion, demonstrating again that expression of CD25 mitigates the difference between the IL-2 superkine and wild-type IL-2 (Fig. 4a and Supplementary Fig. 14b). Thus, the H9 has the desired property that it shows enhanced stimulation towards $CD8^+$ T cells, but not towards $T_{reg}$ cells, compared to wild-type IL-2.

As previously reported, administration of high-dose wild-type IL-2 for 5 days induced substantial pulmonary oedema, which is known to be CD25-dependent[15] (Fig. 4b). Although significantly more stimulatory for cytotoxic $CD8^+$ T cells (Fig. 4a), the H9 IL-2 superkine caused substantially less pulmonary oedema (Fig. 4b).

Given the more favourable properties of H9 in comparison to IL-2, we assessed its ability to stimulate effector functions of cytotoxic T cells in four different tumour models *in vivo*, where high-dose IL-2 administration has been previously shown to result in tumour regression[15,17]. To this end, C57BL/6 mice were injected subcutaneously with B16F10 melanoma cells, followed by administration of either high-dose IL-2, IL-2–anti-IL-2 mAb complexes, or the H9 IL-2 superkine, once tumour nodules became visible and palpable. PBS-treated control mice rapidly developed large subcutaneous tumours reaching a volume of about 1,500 mm$^3$ on day 18 (Fig. 4c). As previously shown, high-dose IL-2 treatment was able to delay tumour growth by as much as 39% on

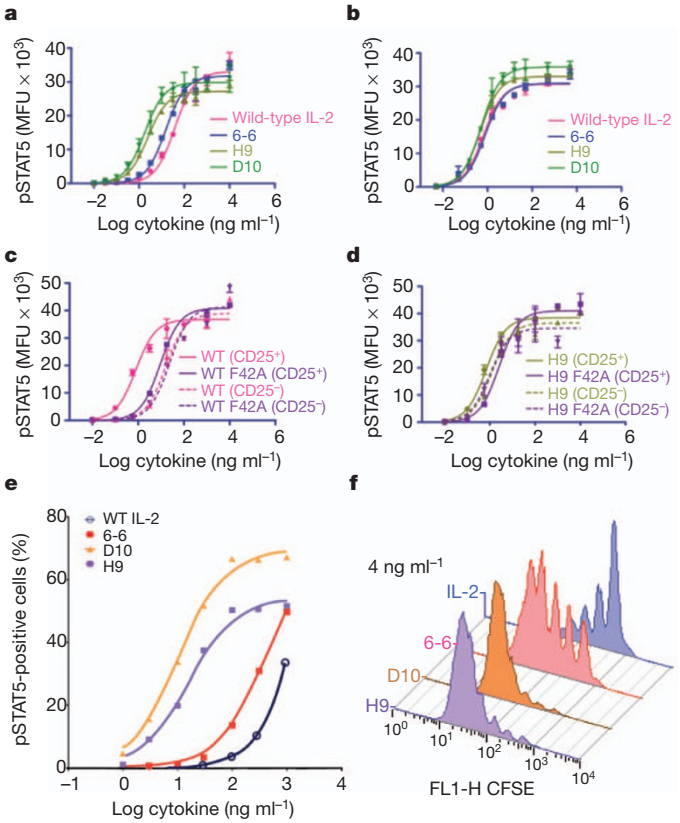


**Figure 3 | Functional properties of the IL-2 superkine on human NK cells *in vitro*.** **a**, **b**, Dose–response curves of STAT5 phosphorylation (pSTAT5) on $CD25^-$ (**a**) and $CD25^+$ (**b**) YT-1 cells with wild-type IL-2 and three IL-2 superkines. MFU, mean fluorescence units. **c**, Dose–response curves of STAT5 phosphorylation on $CD25^+$ (solid curves) and $CD25^-$(dashed curves) YT-1 cells with wild-type IL-2 (pink curves) and IL-2-F42A mutation (purple curves). **d**, Dose–response curves of STAT5 phosphorylation on $CD25^+$ (solid curves) and $CD25^-$(dashed curves) YT-1 cells with H9 (green curves) and H9-F42A mutation (purple curves). **e**, The IL-2 superkines have superior potency over IL-2 on T cells derived from $CD25^{-/-}$ mice as demonstrated by dose–response curves for STAT5 phosphorylation on T cells demonstrating that potency correlates with IL-2Rβ affinity (see also Supplementary Fig. 10). **f**, Proliferation of human naive $CD4^+$ T cells ($CD25^{low}$) reveals similar potency profiles as seen with $CD25^{-/-}$ T cells. Proliferation was measured by carboxyfluorescein succinimidyl ester (CFSE) dilution on day 5 (see also Supplementary Fig. 10). Error bars in **a**–**d** represent s.e.m. of mean fluorescence units for each sample at the indicated cytokine concentration.

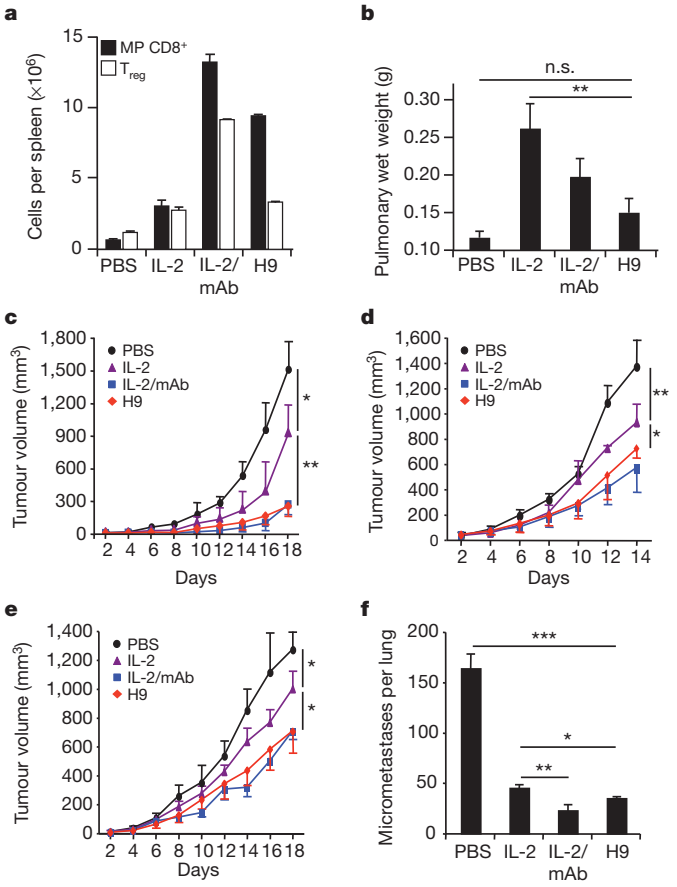


**Figure 4 | Functional and antitumour activities of the IL-2 superkine *in vivo*.** **a**, Total cell counts of host $CD3^+$ $CD8^+$ $CD44^{high}$ memory-phenotype T cells (MP $CD8^+$, closed bars), and host $CD3^+$ $CD4^+$ $CD25^{high}$ T cells ($T_{reg}$, open bars) was determined in the spleens of mice receiving either PBS, 20 μg IL-2, 1.5 μg IL-2–anti-IL-2 mAb complexes (IL-2/mAb), or 20 μg H9 (see also Supplementary Fig. 14). **b**, Pulmonary oedema (pulmonary wet weight) served to assess adverse toxic effects following IL-2 treatment, and was determined by weighing lungs before and after drying. **c**–**f**, C57BL/6 mice ($n = 3$–4 mice per group) were injected either subcutaneously with $10^6$ B16F10 melanoma cells (**c**), $2.5 \times 10^6$ murine colon carcinoma 38 (**d**), $10^6$ Lewis lung carcinoma (**e**), or mice received $3 \times 10^5$ B16F10 melanoma cells intravenously (**f**), followed by daily injections of either PBS, 20 μg IL-2, 1.5 μg IL-2/mAb complexes, or 20 μg H9 for 5 days once subcutaneous tumour nodules became visible and palpable or from day three on for intravenously-injected tumours (see also Supplementary Fig. 15). Shown is mean tumour volume in $mm^3$ (± s.d.) versus time upon tumour inoculation. Error bars represent s.e.m., *P* values refer to comparisons of wild type with the other treatment modalities. $*P < 0.05$; $**P < 0.01$; $***P < 0.001$.

day 18 ($P < 0.05$), whereas IL-2–anti-IL-2 mAb complexes exerted very effective tumour control, reducing tumour growth by more than 80% on day 18 ($P < 0.005$) (Fig. 4c). Significantly, similar to IL-2–anti-IL-2 mAb complexes, mice receiving high-dose H9 showed a dramatic decrease of tumour load on day 18, which was reduced by more than 80% compared to PBS ($P < 0.005$) and by more than 70% compared to wild-type IL-2 ($P < 0.001$) (Fig. 4c). Similar results were obtained using three other tumour models, including murine colon carcinoma and Lewis lung carcinoma injected subcutaneously (Fig. 4d, e) and B16F10 cells administered intravenously (Fig. 4f and Supplementary Fig. 15). Collectively, these data show that the H9 IL-2 superkine is very effective against different tumours, albeit inducing reduced pulmonary oedema.

The practical implications are that this conformational nuance in IL-2 can be exploited for therapy. The IL-2 superkine robustly activates cytotoxic $CD8^+$ T cells and NK cells for potent antitumour immune responses, yet it elicits minimal toxicity, suggesting that the IL-2 superkine could warrant reconsideration for clinical applications of IL-2.

## METHODS SUMMARY

**Yeast display and selection of IL-2.** Error-prone and site-directed libraries of IL-2 were displayed on yeast as previously described[18] and stained with biotinylated IL-2Rβ at successively decreasing concentrations. Staining was detected with streptavidin–phycoerythrin and yeast were separated using paramagnetic anti-phycoerythrin microbeads (Miltenyi; MACS). Enrichment of positively-staining yeast was monitored by flow-cytometry.

**Protein expression, purification and structural determination.** Human IL-2 variants and the ectodomains of IL-2Rβ, IL-2Rγ and CD25 were expressed in Hi5 cells and purified as previously described[11]. Proteins were concentrated to 8–20 mg $ml^{-1}$ and crystallized by vapour diffusion in sitting drops. Diffraction studies were performed at the Stanford Synchrotron Radiation Laboratory and the Advanced Light Source. Crystal structures were solved by molecular replacement with PHASER[19] and refined using PHENIX[20] and COOT[21].

**Mice.** C57BL/6 and Thy1.1-congenic mice on a C57BL/6 background were maintained under specific pathogen-free conditions and used at 3–6 months of age. Experiments were performed in accordance with the Swiss Federal Veterinary Office guidelines and approved by the Cantonal Veterinary Office.

***In vivo* T-cell proliferation.** Carboxyfluorescein succinimidyl ester (CFSE)-labelled $CD44^{high}$ $CD8^+$ T cells ($2 \times 10^6$ to $3 \times 10^6$) from Thy1.1-congenic mice were injected intravenously to Thy1.2-congenic animals. Mice received daily intraperitoneal (i.p.) injections of PBS, 20 μg IL-2, 1.5 μg IL-2–anti-IL-2 mAb complexes, or 20 μg H9 for 5 days. On the sixth day, spleens were removed and analysed by flow cytometry.

**Toxicity.** Pulmonary oedema was determined by measurement of pulmonary wet weight on the sixth day after five daily i.p. injections of PBS, 20 μg IL-2, 1.5 μg IL-2–anti-IL-2 mAb complexes, or 20 μg H9 as previously described[15].

**Tumour models.** B16F10 melanoma cells, Lewis lung carcinoma or murine colon carcinoma 38 cells were injected into mice (3–4 mice per group), as previously reported[15,17]. Treatment consisted of five daily i.p. injections of PBS, 20 μg IL-2, 1.5 μg IL-2–anti-IL-2 mAb complexes, or 20 μg H9.

**Full Methods** and any associated references are available in the online version of the paper at www.nature.com/nature.

**Received 2 October 2011; accepted 20 February 2012.**
**Published online 25 March 2012.**

1. Rochman, Y., Spolski, R. & Leonard, W. J. New insights into the regulation of T cells by $\gamma_c$ family cytokines. *Nature Rev. Immunol.* **9,** 480–490 (2009).
2. Smith, K. A. Interleukin-2: inception, impact, and implications. *Science* **240,** 1169–1176 (1988).
3. Waldmann, T. A. The biology of interleukin-2 and interleukin-15: implications for cancer therapy and vaccine design. *Nature Rev. Immunol.* **6,** 595–601 (2006).
4. Cosman, D. *et al.* Cloning, sequence and expression of human interleukin-2 receptor. *Nature* **312,** 768–771 (1984).
5. Leonard, W. J. *et al.* Molecular cloning and expression of cDNAs for the human interleukin-2 receptor. *Nature* **311,** 626–631 (1984).
6. Nikaido, T. *et al.* Molecular cloning of cDNA encoding human interleukin-2 receptor. *Nature* **311,** 631–635 (1984).
7. Hatakeyama, M. *et al.* Interleukin-2 receptor beta chain gene: generation of three receptor forms by cloned human alpha and beta chain cDNA's. *Science* **244,** 551–556 (1989).
8. Takeshita, T. *et al.* Cloning of the gamma chain of the human IL-2 receptor. *Science* **257,** 379–382 (1992).
9. Boder, E. T. & Wittrup, K. D. Yeast surface display for screening combinatorial polypeptide libraries. *Nature Biotechnol.* **15,** 553–557 (1997).
10. Chao, G. *et al.* Isolating and engineering human antibodies using yeast surface display. *Nature Protocols* **1,** 755–768 (2006).
11. Wang, X., Rickert, M. & Garcia, K. C. Structure of the quaternary complex of interleukin-2 with its α, β, and $\gamma_c$ receptors. *Science* **310,** 1159–1163 (2005).
12. Mott, H. R. *et al.* The solution structure of the F42A mutant of human interleukin 2. *J. Mol. Biol.* **247,** 979–994 (1995).
13. Thanos, C. D., DeLano, W. L. & Wells, J. A. Hot-spot mimicry of a cytokine receptor by a small molecule. *Proc. Natl Acad. Sci. USA* **103,** 15422–15427 (2006).
14. Boyman, O., Kovar, M., Rubinstein, M. P., Surh, C. D. & Sprent, J. Selective stimulation of T cell subsets with antibody-cytokine immune complexes. *Science* **311,** 1924–1927 (2006).
15. Krieg, C., Létourneau, S., Pantaleo, G. & Boyman, O. Improved IL-2 immunotherapy by selective stimulation of IL-2 receptors on lymphocytes and endothelial cells. *Proc. Natl Acad. Sci. USA* **107,** 11906–11911 (2010).
16. Létourneau, S. *et al.* IL-2/anti-IL-2 antibody complexes show strong biological activity by avoiding interaction with IL-2 receptor α subunit CD25. *Proc. Natl Acad. Sci. USA* **107,** 2171–2176 (2010).

17. Rosenberg, S. A., Mule, J. J., Spiess, P. J., Reichert, C. M. & Schwarz, S. L. Regression of established pulmonary metastases and subcutaneous tumor mediated by the systemic administration of high-dose recombinant interleukin 2. *J. Exp. Med.* **161,** 1169–1188 (1985).
18. Rao, B. M., Driver, I., Lauffenburger, D. A. & Wittrup, K. D. Interleukin 2 (IL-2) variants engineered for increased IL-2 receptor α-subunit affinity exhibit increased potency arising from a cell surface ligand reservoir effect. *Mol. Pharmacol.* **66,** 864–869 (2004).
19. McCoy, A. J. *et al. Phaser* crystallographic software. *J. Appl. Crystallogr.* **40,** 658–674 (2007).
20. Adams, P. D. *et al. PHENIX*: building new software for automated crystallographic structure determination. *Acta Crystallogr. D* **58,** 1948–1954 (2002).
21. Emsley, P. & Cowtan, K. *Coot*: model-building tools for molecular graphics. *Acta Crystallogr. D* **60,** 2126–2132 (2004).

**Supplementary Information** is linked to the online version of the paper at www.nature.com/nature.

**Acknowledgements** The authors gratefully acknowledge W. Leonard, R. Levy and R. Schwendener for reagents and discussion. This work was supported by NIH-RO1AI51321 (to K.C.G.), PP00P3-128421 from the Swiss National Science Foundation and KFS-02672-08-2010 from the Swiss Cancer League (both to O.B.), NIH R01-GM062868 (to V.S.P.), MRI-R2 (this award is funded under the American Recovery and Reinvestment Act of 2009 (Public Law 111-5)) (to V.S.P.), NIH-AR050942 (to J.T.L.), NIH U01 DK078123 (to C.G.F.), and NIH U19 AI 082719 (to C.G.F.). A.M.R. was supported by the Stanford Medical Scientist Training Program (NIH-GM07365). K.C.G. is an Investigator of the Howard Hughes Medical Institute.

**Author Contributions** A.M.L. performed *in vitro* evolution and contributed to preparation of the manuscript. D.L.B. produced recombinant proteins, determined crystal structures, and carried out surface plasmon resonance analysis. A.M.R. carried out cellular and signalling assays, biophysical measurements and contributed to preparation of the manuscript. C.K. carried out *in vivo* experiments, analysed data and contributed to preparation of the manuscript; M.E.R. carried out *in vivo* experiments in mice. I.M. analysed cell-signalling data. G.R.B., P.N. and V.S.P. carried out and analysed molecular dynamics simulations. J.T.L., L.S. and C.G.F. performed and analysed T-cell signalling experiments. O.B. designed and supervised *in vivo* experiments, analysed data and contributed to preparation of the manuscript. K.C.G. conceived of the project, analysed data, supervised execution of the project, and prepared the manuscript.

**Author Information** Atomic coordinates and structure factors for the reported crystal structures have been deposited with the Protein Data Bank under accession codes 3QAZ and 3QB1. Reprints and permissions information is available at www.nature.com/reprints. The authors declare competing financial interests: details accompany the full-text HTML version of the paper at www.nature.com/nature. Readers are welcome to comment on the online version of this article at www.nature.com/nature. Correspondence and requests for materials should be addressed to K.C.G. (kcgarcia@stanford.edu) or O.B. (onur.boyman@uzh.ch).

## METHODS

**Yeast display of wild-type IL-2.** Human IL-2 DNA was cloned into the vector pCT302 and displayed on the *Saccharomyces cerevisiae* strain EBY100 as previously described[18]. Individual colonies of IL-2 yeast were grown overnight at 30 °C in SDCAA liquid media and induced in SGCAA liquid media for 2 days at 20 °C. The yeast were stained with tetramerized biotinylated IL-2Rβ (b-IL-2Rβ), biotinylated IL-2Rγ (b-IL-2Rγ), or b-IL-2Rβ in the presence of b-IL-2Rγ. IL-2Rβ tetramers were formed by incubating 2 μM b-IL-2Rβ with 470 nM SAV-PE (streptavidin–phycoerythrin conjugate, Invitrogen) in phosphate buffered saline supplemented with 0.5% BSA and 2 mM EDTA (PBE) for 15 min on ice. Analysis was performed on an Accuri C6 flow cytometer.

**Error-prone PCR IL-2 library construction and selection.** Human IL-2 DNA was subjected to error-prone PCR using the GeneMorphII kit (Stratagene). The two user-determined variables in the kit were the starting concentration of DNA template and the number of cycles. We used 100 ng template and 30 cycles in an effort to maximize the number of errors. The primers used for error-prone PCR were 5′-GCACCTACTTCAAGTTCTAC-3′ for the forward primer and 5′-GC CACCAGAGGATCC-3′ for the reverse primer. The PCR product was further amplified using primers containing sequence homology to pCT302 for recombination inside the yeast: forward primer 5′-AGTGGTGGTGGTGGTTCTGG TGGTGGTGGTTCTGGTGGTGGTGGTTCTGCTAGCGCACCTACTTCAAG TTCTAC-3′ and reverse primer 5′-ACACTGTTGTTATCAGATCTCGAGCAA GTCTTCTTCGGAGATAAGCTTTTGTTCGCCACCAGAGGATCC-3′. Insert DNA was combined with linearized vector backbone and EBY100 yeast and electroporated as previously described[10]. The electroporations yielded a library of $1 \times 10^8$ transformants. Selections were performed using magnetic activated cell sorting (MACS, Miltenyi). First-round selection was performed with $1 \times 10^9$ yeast, approximately tenfold coverage of the number of transformants. Yeast were stained with 10 ml of 500 nM IL-2Rβ SAV-PE tetramers in PBE for 2 h with slow rotation at 4 °C. Cells were pelleted at 5,000*g* for 5 min, buffer aspirated, and washed with PBE. The pellet was resuspended in 9.6 ml PBE and 400 μl Miltenyi anti-PE microbeads, incubated for 20 min with slow rotation at 4 °C, pelleted, and washed with 14 ml PBE. The yeast were then resuspended in 5 ml PBE and magnetically separated by a Miltenyi LS column, following the manufacturer's protocols. Subsequent rounds of selection used $1 \times 10^8$ yeast cells, successively lower concentrations of monomeric IL-2Rβ for increased selection stringency, and 100 μl of Miltenyi microbeads to capture labelled yeast-displayed IL-2 variants.

**Site-directed hydrophobic core IL-2 library construction and selection.** The site-directed library was created by assembly PCR of 13 primers, two of which contained the following degenerate codons: Q74 = MRS, L80 = NTC, R81 = NNK, L85 = NTC, I86 = NTC, I89 = NTC, I92 = NTC, V93 = NTC. The primers used for assembly PCR were: 5′-GCACCTACTTCAAGTTCTACAA AGAAAACACAGCTACAACTGGAGCA-3′, 5′-CAAAATCATCTGTAAATC CAGAAGTAAATGCTCCAGTTGTAGCTGTG-3′, 5′-GGATTTACAGATGA TTTTGAATGGAATTAATAATTACAAGAATCCCA-3′, 5′-AACTTAGCTGT GAGCATCCTGGTGAGTTTGGGATTCTTGTAATTATT-3′, 5′-GGATGCTC ACA**GCT**AAGTTTTACATGCCCAAGAAGGCCACAGAACTG-3′, 5′-GTTC TTCTTCTAGACACTGAAGATGTTTCAGTTCTGTGGCCTTCTTG-3′, 5′-CA GTGTCTAGAAGAAGAACTCAAACCTCTGGAGGAAGTGCTAAATTTA-3′, 5′-GTGAAAGTTTTTGCT***SYK***AGCTAAATTTAGCACTTCCTCC-3′, 5′-AG CAAAAACTTTCAC***NTCNNK***CCCAGGGAC***NTCNTC***AGCAAT***NTC***AACG TA***NTCNTC***CTGGAACTAAAGGGATC-3′, 5′-CATCAGCATATTCACACA TGAATGTTGTTTCAGATCCCTTTAGTTCCAG-3′, 5′-ATGTGTGAATATG CTGATGAGACAGCAACCATTGTAGAATTTCTGAACA-3′, 5′-AGATGAT GCTTTGACAAAAGGTAATCCATCTGTTCAGAAATTCTACAAT-3′, 5′-TT TTGTCAAAGCATCATCTCAACACTAACTGGATCCTCTGGTGGC-3′. The assembly PCR reaction was performed using *Pfu* DNA polymerase (Stratagene). The product DNA was further PCR-amplified using the same primers as the error-prone library. Electroporation of insert DNA and linearized vector into EBY-100 yeast yielded a library of $1.4 \times 10^8$ transformants. Selection of the site-directed library was performed as with the error-prone library, except tenfold lower concentrations of monomeric IL-2Rβ were used.

**Protein expression and purification.** Human IL-2 variants (amino acids 1–133), the IL-2Rβ ectodomain (amino acids 1–214), IL-2Rγ (amino acids 34–232) and CD25 (amino acids 1–217) were expressed and purified from Hi5 cells as previously described[11]. For biotinylated receptor expression, IL-2Rβ and IL-2Rγ with a C-terminal biotin acceptor peptide (BAP)-LNDIFEAQKIEWHE were co-expressed with BirA ligase with excess biotin (100 μM). CD25 was biotinylated at its free cysteine by incubation with biotin–maleimide (Sigma). For crystallization, receptor constructs were co-expressed with *N*-linked glycosylation sites IL-2Rβ residues Asn 3, 17, 45, and IL-2Rγ residues Asn 53 mutated to Gln. IL-2 proteins used for crystallization were expressed with *N*-linked glycosylation inhibitor tunicamycin (0.2 μg ml$^{-1}$). Proteins were treated overnight with carboxypeptidase-A followed by size-exclusion chromatography.

**Surface plasmon resonance.** SPR experiments were conducted on a Biacore T100 instrument at 25 °C. All data was analysed using the Biacore T100 evaluation software version 2.0 with a 1:1 Langmuir binding model. Experiments used a Biacore SA sensor chip (GE Healthcare). Biotinylated receptors were captured at a low density ($R_{max} \approx 30$ response units) and kinetic runs were conducted at 40 μl min$^{-1}$ to eliminate mass transport and rebinding artefacts. An unrelated biotinylated protein was immobilized as a reference surface. All measurements were made using threefold serial dilutions of IL-2 variants (GE Healthcare, 0.01% BSA). IL-2Rβ was regenerated using 10 mM sodium acetate (pH 5.5) and 1 M $MgCl_2$. CD25 was regenerated using 1 M NaCl. Kinetic data was determined using 120 s to 190 s of IL-2 variant association and 20 s to 600 s disassociation.

**Isothermal titration calorimetry.** Calorimetry experiments with the H9 and D10 IL-2 superkines with IL-2Rβ were conducted as previously described[22]. Briefly, titrations were performed on a VP-ITC calorimeter (MicroCal) at 15 °C. Prior to titration, protein and reference water was degassed for 10 min. All samples were extensively dialysed in 10 mM HEPES pH 7.4, 150 mM NaCl (HBS) before titration to minimize heat of dilution effects. Data were processed and analysed using the MicroCal Origin 5.0 software.

**Crystallization and data collection.** IL-2 D10 crystals were grown in sitting drops at 22 °C from 50 mM HEPES (pH 7.2), 200 mM NaCl and 30% PEG-4000. A 3.1 Å data set was collected under cryo-cooled conditions (20% glycerol) at beamline 11-1 at the Stanford Synchrotron Radiation Laboratory. IL-2 D10 ternary crystals were grown from 100 mM Bis-Tris (pH 5.5), 200 mM $NH_4SO_4$ and 25% PEG-3350. A cryo-cooled 3.8 Å data set was collected at beamline 8-2 at the Advanced Light Source. Diffraction data were processed using HKL2000. Data processing statistics can be found in Supplementary Table 1.

**Structure determination and refinement.** The IL-2 D10 and IL-2 D10 ternary crystal structures were solved by molecular replacement with the program PHASER[19] using the coordinates of IL-2 (PDB ID 1M47) and the quaternary complex (PDB ID 2B5I), respectively, and refined with PHENIX[20] and COOT[21] (Supplementary Table 1). Bulk solvent flattening was used for solvent correction in both structures. For both the IL-2 D10 free structure and the ternary complex non-crystallographic symmetry (NCS) restraints (not constraints) were used for initial stages of the refinement. Coordinate refinement strategies included rigid body, restrained individual, group atomic displacement parameters (ADP) and torsion-simulated annealing. The final rounds of refinement removed all NCS restraints for minimization and a round of individual ADP refinement.

Ramachandran analysis was performed with MolProbity[23]. Buried surface area values were calculated using the Protein Interfaces, Surfaces, and Assemblies (PISA) software[24]. IL-2 D10 consisted of eight chains with chain A displayed in the paper. The IL-2 D10 ternary complex contained 36 chains comprising 12 ternary complexes. The paper figures are from chains A, B and C. All structural figures and overlays were prepared using PyMOL[25].

**Tissue culture and magnetic purification of CD25$^+$ YT-1 cells.** YT-1 and CD25$^+$ YT-1 cells were cultured in RPMI 1640 medium supplemented with 10% fetal bovine serum, 2 mM L-glutamine, minimum non-essential amino acids, sodium pyruvate, 25 mM HEPES, and penicillin-streptomycin (Gibco). CD25$^+$ YT-1 cells were purified as follows: $1 \times 10^7$ cells were washed with FACS buffer (phosphate buffered saline + 2% bovine serum albumin) and stained with PE-conjugated anti-human CD25 (1:20; Biolegend) in 1 ml FACS buffer for 20 min at 4 °C. The stained cells were labelled with 200 μl paramagnetic microbeads coupled to anti-PE IgG and separated with an LS MACS separation column according to the manufacturer's instructions (Miltenyi Biotec). Eluted cells were re-suspended in complete RPMI medium at a concentration of $1 \times 10^5$ cells per ml and expanded for subsequent experiments. Enrichment of cells was monitored via flow cytometry with the FL-2 channel using an Accuri C6 flow cytometer.

**YT-1 dose–response experiments and phospho-flow cytometric analysis.** $2 \times 10^5$ CD25$^+$ or CD25$^-$ YT-1 cells were washed with FACS buffer and re-suspended in 200 μl FACS buffer with the indicated concentration of IL-2 variant per well in a 96-well plate. Cells were stimulated for 20 min at room temperature and then fixed by addition of formaldehyde to 1.5% and incubated for 10 min. Cells were permeabilized with 100% ice-cold methanol for 20 min on ice, followed by incubation at −80 °C overnight. Fixed, permeabilized cells were washed with excess FACS buffer and incubated with 50 μl Alexa647-conjugated anti-STAT5 pY694 (BD Biosciences) diluted 1:20 in FACS buffer for 20 min. Cells were washed twice in FACS buffer and mean cell fluorescence determined using the FL-4 channel of an Accuri C6 flow cytometer. Dose–response curves and $EC_{50}$ values were calculated in GraphPad Prism after subtracting the mean cell fluorescence of unstimulated cells.

For 'on-yeast' stimulation experiments, the same protocol was used with the following modifications. Induced yeast were washed twice in FACS buffer and

mixed with the $2 \times 10^5$ YT cells at the indicated ratios for 20 min in FACS buffer at room temperature. Cells were then fixed, permeabilized and stained as described above.

**T cell isolation and proliferation for phospho-flow cytometric analysis.** Human and mouse CD4 T cells were prepared from peripheral blood mononuclear cells (PBMC, Stanford Blood Bank) and spleens and lymph nodes of BALB/C mice, respectively, using antibody-coated CD4 T-cell isolation magnetic beads (Stem Cell Technologies and Miltenyi Biotec). For naive cell stimulation assays, cells were used immediately. For generation of *in vitro* 'experienced' T cells, wells were pre-coated with secondary antibody (Vector Labs) in bicarbonate buffer, pH 9.6 before coating plates with anti-CD3 (OKT3 for human, 2C11 for mouse, eBiosciences) at 100 ng $ml^{-1}$. T cells were seeded at $0.1 \times 10^6$ cells per well with soluble anti-CD28 (CD28.2 for human, 37.51 for mouse, eBiosciences). Cells were cultured for 3 days with full T-cell receptor stimulation, followed by 2 days rest in conditioned media and 2 days rest in fresh culture media. Prior to use, live cells were collected by Lympholyte-M (Cederlane) centrifugation and counted.

***In vivo* studies.** C57BL/6 and Thy1.1-congenic mice on a C57BL/6 background (both from Charles River) were maintained under specific pathogen-free conditions and used at 3–6 months of age. Experiments were performed in accordance with the Swiss Federal Veterinary Office guidelines and approved by the Cantonal Veterinary Office.

Cell suspensions of spleen were prepared according to standard protocols[14] and stained for analysis by flow cytometry using phosphate-buffered saline (PBS) containing 4% fetal calf serum and 2.5 mM EDTA. Fluorochrome-conjugated monoclonal antibodies (mAbs) (from BD Biosciences unless otherwise stated) were used against: CD3 (145-2C11, eBioscience), CD4 (RM4-5, Caltag Laboratories), CD8a (53-6.7), CD25 (PC61), CD44 (IM7, eBioscience), NK1.1 (PK136), and Thy1.1 (HIS51, eBioscience). At least 100,000 viable cells were acquired on a BD FACSCanto II flow cytometer and analysed using FlowJo software (TriStar Inc.).

To prepare IL-2–anti-IL-2 mAb complexes, recombinant human IL-2 (rhIL-2) and anti-human IL-2 mAb were premixed at a 2:1 molar ratio using 15,000 international units of recombinant human IL-2, as previously described[15]. Recombinant human IL-2 and anti-human IL-2 mAb clone 5355 (MAB602) were obtained from R&D Systems.

T-cell subsets were obtained by negative T-cell enrichment (StemCell Technologies). Where indicated, purified cells were labelled with carboxyfluorescein diacetate succinimidyl ester (CFSE, Molecular Probes), as previously published[14]. $2 \times 10^6$ to $3 \times 10^6$ $CD8^+$ T cells from Thy1.1-congenic wild-type mice enriched for $CD44^{high}$ memory-phenotype cells were injected intravenously (i.v.) to Thy1.2-congenic wild-type mice. Starting on the day of adoptive cell transfer, age- and gender-matched mice received daily intraperitoneal (i.p.) injections of either PBS, 20 μg wild-type human IL-2, 20 μg H9, or 1.5 μg human IL-2–anti-IL-2 mAb complexes for 5 consecutive days. 6 days after adoptive cell transfer, spleens were removed and analysed by flow cytometry.

Pulmonary wet weight was determined according to previously established protocols[15]. In brief, wild-type mice received daily i.p. injections of either PBS, 20 μg wild-type human IL-2, 20 μg H9, or 1.5 μg IL-2–anti-IL-2 mAb complexes for 5 consecutive days as described above. On day 6, lungs were removed and weighed before and after drying overnight at 58 °C under vacuum. Pulmonary wet weight was calculated by subtracting initial pulmonary weight from lung weight after dehydration.

To generate subcutaneous tumours, as indicated either $10^6$ B16F10 melanoma (from ATCC), $10^6$ Lewis lung carcinoma (provided by R. Schwendener), or $2.5 \times 10^6$ murine colon carcinoma 38 (provided by R. Schwendener) cells were injected in 100 μl DMEM into the upper dermis of the back of mice (3–4 mice per group), as previously established[15]. Treatment consisted of five daily injections of either PBS, 20 μg IL-2, 1.5 μg IL-2–anti-IL-2 mAb complexes, or 20 μg H9, and was started 1 day after tumour nodules were clearly visible and palpable at a volume of approximately 50–55 $mm^3$. For the generation of lung metastases, $3 \times 10^5$ B16F10 cells in 300 μl DMEM were injected into the tail vein, as previously shown[15]. Treatment was as above and was started on day 3 after tumour inoculation. On day 16 after injection, lungs were perfused, harvested and fixed in Fekete's solution (70% ethanol, 3.7% paraformaldehyde, 0.75 M glacial acetic acid), followed by dissection of lungs and counting of pulmonary micrometastases. Differences between groups were examined for statistical significance by using a one-way analysis of variance (ANOVA) with Bonferroni post-test correction.

**Molecular dynamics simulations and MSM.** We used MODELLER[26] with the default settings to create five starting conformations for simulations from each of three IL-2 structures (PDB ID 3INK, 1M47 and 1Z92; refs 27–29), and D10 with both the wild-type IL-2 sequence and the D10 sequence. The five conformations for a particular sequence/structure differ only where residues are missing or mutated.

Molecular dynamics simulations were run with Gromacs 4.5.2 (ref. 30) using the AMBER03 force field[31]. Each structure was placed in a dodecahedral box of about 7.1 by 7.1 by 5 nm and solvated with approximately 7,650 TIP3P water molecules. Conformations were first minimized with a steepest descent algorithm using a tolerance of 1,000 kJ $mol^{-1}$ $nm^{-1}$ and a step size of 0.01 nm. A 1-nm cutoff was used for Coulombic and Van der Waals interactions and a grid-based neighbour list. Conformations were then equilibrated at 300 K and 1 bar by holding protein atoms fixed and allowing the surrounding water to relax for 500 ps with a 2 fs time-step. All bonds were constrained with the LINCS algorithm[32]. Centre of mass motion was removed at every step and a grid-based neighbour list with a cutoff of 1.5 nm was updated every 10 steps. For electrostatics, we used fourth order PME[33] with a cutoff of 1.5 nm for Coulombic interactions, a Fourier spacing of 0.08 nm, and a tolerance of $1 \times 10^{-5}$. A hard cutoff of 1.2 nm was used for Van der Waals interactions with a switch starting at 1 nm. The temperature was controlled with two Nose–Hoover thermostats[34] applied to the protein and solvent respectively with a time constant of 0.5 ps. The pressure was controlled with an isotropic Berenson barostat[35] applied to the entire system with a time constant of 0.5 ps and a compressibility of $4.5 \times 10^{-5}$ $bar^{-1}$. Long-range corrections were applied to energy and pressure. Production simulations up to 40 ns duration used the same parameters as for equilibration, with the exception that the protein atoms were no longer held fixed.

We used MSMBuilder[36] to construct an MSM with a 4-ns lag time. Based on previous work on protein folding[37], we chose to create 70 clusters (microstates) using a k-centres algorithm and the r.m.s.d. between pairs of conformations. All $C_\alpha$ and $C_\beta$ atoms were used for the r.m.s.d., thereby allowing different sequences to be used in the same clustering. Thermodynamic and kinetic properties were extracted from the MSM's eigenvalues and eigenvectors[38,39].


22. Rickert, M., Boulanger, M. J., Goriatcheva, N. & Garcia, K. C. Compensatory energetic mechanisms mediating the assembly of signaling complexes between interleukin-2 and its α, β, and $\gamma_c$ receptors. *J. Mol. Biol.* **339,** 1115–1128 (2004).
23. Davis, I. W. *et al.* MolProbity: all-atom contacts and structure validation for proteins and nucleic acids. *Nucleic Acids Res.* **35,** W375–W383 (2007).
24. Krissinel, E. & Henrick, K. Inference of macromolecular assemblies from crystalline state. *J. Mol. Biol.* **372,** 774–797 (2007).
25. DeLano, W. L. The PyMOL Molecular Graphics System (DeLano Scientific, 2002).
26. Eswar, N. *et al. Comparative Protein Structure Modeling With MODELLER. Current Protocols in Bioinformatics*. Vol. 15 5.6.1-5.6.30 (Wiley, 2006).
27. Bazan, J. F. Unraveling the structure of IL-2. *Science* **257,** 410–413 (1992).
28. Arkin, M. R. *et al.* Binding of small molecules to an adaptive protein–protein interface. *Proc. Natl Acad. Sci. USA* **100,** 1603–1608 (2003).
29. Rickert, M., Wang, X., Boulanger, M. J., Goriatcheva, N. & Garcia, K. C. The structure of interleukin-2 complexed with its alpha receptor. *Science* **308,** 1477–1480 (2005).
30. Hess, B., Kutzner, C., van der Spoel, D. & Lindahl, E. GROMACS 4: algorithms for highly efficient, load-balanced, and scalable molecular simulation. *J. Chem. Theory Comput.* **4,** 435–447 (2008).
31. Duan, Y. *et al.* A point-charge force field for molecular mechanics simulations of proteins based on condensed-phase quantum mechanical calculations. *J. Comput. Chem.* **24,** 1999–2012 (2003).
32. Hess, B. P-LINCS: a parallel linear constraint solver for molecular simulation. *J. Chem. Theory Comput.* **4,** 116–122 (2008).
33. Essmann, U. *et al.* A smooth particle mesh Ewald method. *J. Chem. Phys.* 103**,** 8577–8593 (1995).
34. Hoover, W. G. Canonical dynamics: equilibrium phase-space distributions. *Phys. Rev. A* **31,** 1695–1697 (1985).
35. Berendsen, H. J. C., Postma, P. M., van Gunsteren, W. F., DiNola, A. & Haak, J. R. Molecular dynamics with coupling to an external bath. *J. Chem. Phys.* **81,** 3684–3690 (1984).
36. Bowman, G. R., Huang, X. & Pande, V. S. Using generalized ensemble simulations and Markov state models to identify conformational states. *Methods* **49,** 197–201 (2009).
37. Bowman, G. R., Beauchamp, K. A., Boxer, G. & Pande, V. S. Progress and challenges in the automated construction of Markov state models for full protein systems. *J. Chem. Phys.* **131,** 124101 (2009).
38. Bowman, G. R., Huang, X. & Pande, V. S. Network models for molecular kinetics and their initial applications to human health. *Cell Res.* **20,** 622–630 (2010).
39. Noé, F. & Fischer, S. Transition networks for modeling the kinetics of conformational change in macromolecules. *Curr. Opin. Struct. Biol.* **18,** 154–162 (2008).